Article
Chinese Science Bulletin
Geochemistry
October 2013 Vol.58 No.28-29: 3546–3563
doi: 10.1007/s11434-013-5792-4

Episodic crustal anatexis and the formation of Paiku composite leucogranitic pluton in the Malashan Gneiss Dome, Southern Tibet

GAO LiE[1*], ZENG LingSen[1], HOU KeJun[2], GUO ChunLi[2], TANG SuoHan[1], XIE KeJia[3], HU GuYue[2] & WANG Li[1]

[1] *State Key Laboratory of Continental Tectonics and Dynamics, Institute of Geology, Chinese Academy of Geological Sciences, Beijing 100037, China;*
[2] *Institute of Mineral Resources, Chinese Academy of Geological Sciences, Beijing 100037, China;*
[3] *Non-Ferrous Mineral Exploration Engineering Research Center of Henan Province, Zhengzhou 450016, China*

Received December 18, 2012; accepted February 26, 2013; published online April 16, 2013

The Paiku composite leucogranitic pluton in the Malashan gneiss dome within the Tethyan Himalaya consists of tourmaline leucogranite, two-mica granite and garnet-bearing leucogranite. Zircon U-Pb dating yields that (1) tourmaline leucogranite formed at 28.2±0.5 Ma and its source rock experienced simultaneous metamorphism and anatexis at 33.6±0.6 Ma; (2) two-mica granite formed at 19.8±0.5 Ma; (3) both types of leucogranite contain inherited zircon grains with an age peak at ~480 Ma. These leucogranites show distinct geochemistry in major and trace elements as well as in Sr-Nd-Hf isotope compositions. As compared to the two-mica granites, the tourmaline ones have higher initial Sr and zircon Hf isotope compositions, indicating that they were derived from different source rocks combined with different melting reactions. Combined with available literature data, it is suggested that anatexis at ~35 Ma along the Himalayan orogenic belt might have triggered the initial movement of the Southern Tibetan Detachment System (STDS), and led to the tectonic transition from compressive shortening to extension. Such a tectonic transition could be a dominant factor that initiates large scale decompressional melting of fertile high-grade metapelites along the Himalayan orogenic belt. Crustal anatexis at ~28 Ma and ~20 Ma represent large-scale melting reactions associated with the movement of the STDS.

Himalayan orogenic belt, Northern Himalayan Gneiss Domes, leucogranite, crustal anatexis, tectonic transition

Citation: Gao L E, Zeng L S, Hou K J, et al. Episodic crustal anatexis and the formation of Paiku composite leucogranitic pluton in the Malashan Gneiss Dome, Southern Tibet. Chin Sci Bull, 2013, 58: 3546–3563, doi: 10.1007/s11434-013-5792-4

Cenozoic leucogranites within the Himalayan collisional orogenic belt is one of the type examples of S-type granite worldwide. Knowledge of their geochemical nature and timing of formation could not only potentially promote our understanding of the melting behaviors of deep crustal rocks during collisional orogenic processes, but also provide key geochemical and temporal constraints on the tectonic evolution of the Himalayan orogenic belt. Earlier studies on these Cenozoic granites have demonstrated that most of them formed at 27–10 Ma [1–4] and were derived from in situ partial melting of high-grade metapelites [3,5,6]. Experimental results have demonstrated that partial melting of Formation-I kyanite-bearing metapelite indeed can produce melts with elemental and isotopic compositions resembling the Himalayan Cenozoic leucogranites [6,7], however, increasing number of updated studies have documented that episodic anatexis occurred in the Northern Himalayan Gneiss Domes (NHGD) as well as in the High Himalayan Crystalline Sequence (HHCS) since the continental collision between India and Eurasia. These anatectic episodes include (1) dehydration melting of a source consisting dominantly of amphibolite with subordinate pelitic gneiss at thickened crustal conditions [8–14]. These melting events are represented by older than 35 Ma peraluminous granitoids with

*Corresponding author (email: liegao09@gmail.com)

relatively high Na/K and Sr/Y ratios; (2) fluid-present melting of metapelite since ~38 Ma to produce granitic melts with high CaO and Sr contents and low Rb/Sr ratios [15–18]; and (3) late Eocene to early Oligocene anatexis recorded in syn-collision leucogranites and migmatites in the Gyirong area and the Mabja Gneiss Dome [19–21]. A large number of studies have demonstrated that metapelites are fertile and could undergo progressive partial melting with variations in temperature, pressure, and water content, which leads to the formation of granites with different geochemical characteristics in major and trace element as well as in isotope (e.g. Sr, Nd) geochemistry [4,6,7,16,18,22,23]. Therefore, these granites provide an important probe to investigate how the middle-lower crustal rocks respond to the tectonic evolution of orogenic belts. Data summarized above indicate that partial melting in the Himalayan orogenic belt could be traced back to the middle Eocene and sources and mechanisms of anatexis are more complex than previous thought, therefore, more studies are required to determine the geochemical nature and the timing of partial melting processes along the Himalayan orogen in order to refine our understanding on the deep processes in large orogenic belts and draw broader tectonic implications.

Limited studies have been performed on the Malashan Gneiss Dome (MGD) in the west of NHGD. Aoya et al. [24] and Kawakami et al. [25] had investigated the nature and sequence of metamorphism and deformation in the wall-rocks of Malashan granites and shown that the wall-rocks had experienced contact metamorphism due to the intrusion of the Malashan granite. Zircon U-Pb and mica $^{40}Ar/^{39}Ar$ dating results reported by Aoya et al. [26], Kawakami et al. [25] and Zhang et al. [21] suggested that the Malashan granite crystallized over a long time span (~10 myr), which could be due to mixing ages from domains straddling across different growth zonings. To the south of the Malashan granite, recent field investigations found that the Paiku leucogranite is a composite pluton rather than a single one [25,26]. This pluton consists of tourmaline leucogranite, two-mica leucogranite, and garnet-bearing granite. In order to narrow down the formation age and characterize the mineral and geochemical composition of this leucogranitic pluton, we have sampled along traversals across this pluton as shown in Figure 1(b) and conducted bulk-rock major and trace element and radiogenic isotope (Sr and Nd), as well as

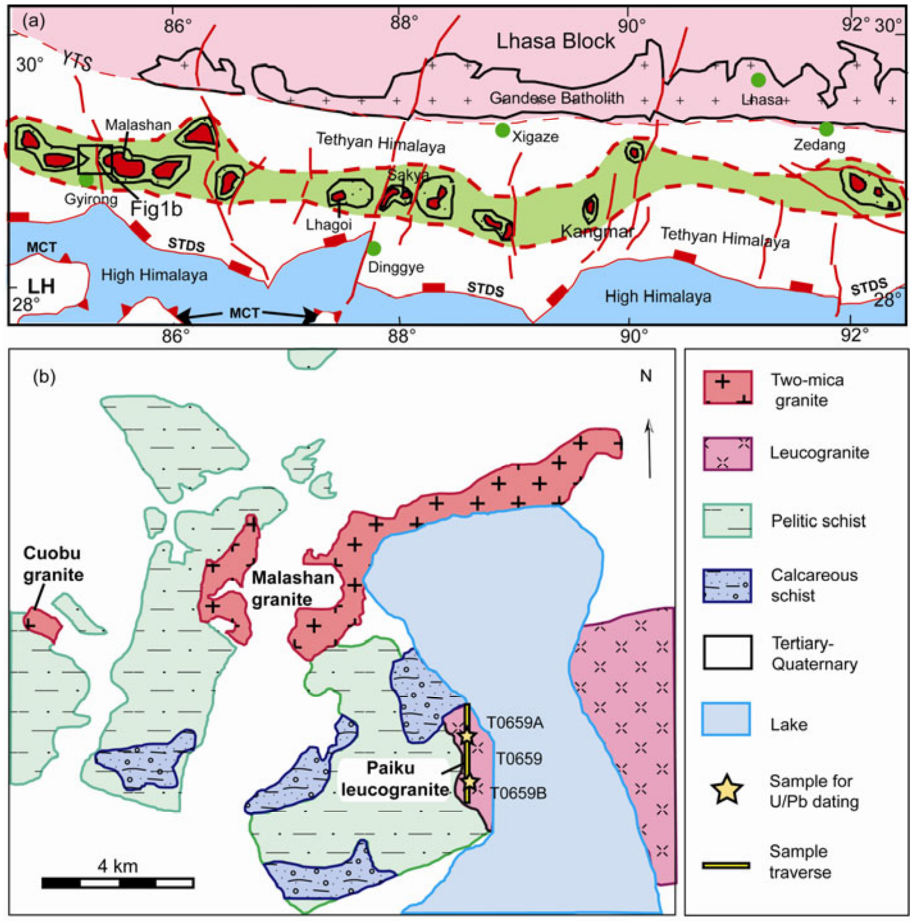

Figure 1 (a) Simplified geologic map of the Himalayan orogenic belt, southern Tibet (after Zeng et al. [12]); (b) simplified geological map of the Malashan Gneiss Dome (after Aoya et al. [24]). YTS, Yarlung-Tsangpo suture; STDS, Southern Tibet Detachment System; MCT, Main Center Thrust; MBT, Main Boundary Thrust; LH, Lower Himalayan Crystalline Sequence.

LA-MC-ICP-MS zircon U/Pb and Hf isotope analyses on tourmaline- and two-mica granites.

1 Geological setting and sample descriptions

Leucogranites in the Himalayan orogen are distributed along two sub-parallel belts, HHCS and NHGD, which are separated by the Southern Tibetan Detachment System (STDS) (Figure 1(a)). Granites, migmatites, and high-grade metamorphic rocks are important components within these two belts and record distinct types of metamorphism and partial melting reactions of middle-lower crustal materials in response to the tectonic evolution of the Himalayan orogen [1,4,8,13,14,16,26–29]. NHGD within the Tethyan Himalaya consists of a series of semi-continuous oval shape gneiss dome. These domes share similar features and consist of high-grade metamorphic rocks and intruded granites in the core and low grade metamorphic or unmetamorphosed sedimentary toward the margin. All these rock units are separated by ductile detachment fault. Except for the Kangmar Dome, all granites within the NHGD are younger than ~44 Ma [3,4,8,12,13,16,19,26,30]; whereas the granites within the HHCS formed at 37–10 Ma and are characterized by apparently lower melt temperature [3].

Granites in the Malashan Gneiss Dome include the Cuobu two-mica granite (TMG), Malashan two-mica granite (TMG) and Paiku leucogranite (Figure 1(b)). These granites intruded into pelitic and calcareous schist mapped as Jurassic and Cretaceous in age [31]. Presence of andalusite and skarn formation in the metasediments within the proximity of these granites indicates relatively intensive contact metamorphism in the sedimentary wall-rocks induced by the emplacement of granitic plutons [24,25]. The Paiku composite leucogranite pluton consists of tourmaline leucograntie, two-mica granite and garnet-bearing leucogranite. Detailed field investigations on the cross-cutting relationship between these leucogranites indicate that the pelitic sediments were first intruded by the tourmaline leucogranites, followed by the intrusion of the Paiku TMG, and finally the Malashan TMG. Major features in the Malashan dome include: (1) the Malashan TMG experienced strong deformation, but others not [24,26,32]; (2) presence of Barrovian-type metamorphism with grade increasing toward the granite core [25]; (3) development of two major episodes of ductile deformation represented by earlier top-to-the south D1 and later top-to-the north D2 fabric, respectively. The intensity of D2 fabric increased toward the granite contact; (4) roughly north-south D2 flow direction indicated by the D2 stretching lineation; and (5) no sillimanite or migmatite found in the metasedimentary wall-rocks implies relatively lower metamorphic grade than the other gneiss domes [24,26]. The least deformed Cuobu granite has strikingly similar bulk chemical compositions to those of the Malashan granite, but is apparently different from the Paiku leucogranite [26]. Sensitive high-resolution ion microprobe zircon U-Pb dating yielded that the Cuobu TMG formed at 26.0–13.7 Ma [26], Malashan TMG at 30.2–17.2 Ma [21,26]. ^{40}Ar-^{39}Ar dating on muscovite and biotite yielded similar cooling ages of 17.6–15.3 Ma for the Cuobu and Malashan TMG, respectively [21,26]. The Paiku leucogranite formed at 22.2–16.2 Ma, and ^{40}Ar-^{39}Ar cooling age is 15.9 Ma [25].

Leucogranites within the Paiku pluton contain largely similar mineral assemblage and textures with variations in relative proportion in muscovite. All three types of leucogranite consist of quartz, plagioclase, muscovite, and accessory phases of zircon, apatite and monazite. The tourmaline leucogranite contains more muscovite (~20%) than others (<15%). The tourmaline leucogranites contain abundant (up to ~10%) large, euhedral, and compositionally zoned tourmaline grains (Figure 2(b)), in contrast, two-mica granite contains 5%–10% biotite (Figure 2(c)) and garnet-bearing leucogranite contains up to 2% large and subhedral garnet grains (Figure 2(d)). Sample T0659-A is a representative tourmaline leucogranite and has a similar mineral assemblage and microstructure to sample T0659-1 to T0659-6, whereas T0659-B is two-mica granite similar to sample T0659-11 to T0659-14.

2 Analytical methods

2.1 LA-MC-ICP-MS zircon U-Pb dating

Zircons were separated from representative sample T0659-A and sample T0659-B from Paiku Cuo (Figure 1(b)) by using standard heavy-liquid and magnetic techniques, and then handpicked under a binocular microscope. The selected grains were embedded in 25 mm epoxy discs and grounded to approximately half of their thickness. The internal growth structure of zircon grains was revealed by cathodoluminescence (CL) and BSE imaging technique. CL images were obtained at the Beijing SHRIMP Centre, Chinese Academy of Geological Sciences (CAGS). BSE images were obtained with a JSM-5610LV scanning microscope at the Institute of geology, CAGS.

The zircons were analyzed for U, Th, and Pb using LA-MC-ICP-MS at Key Laboratory of Metallogeny and Mineral Assessment, Institute of Mineral Resources, CAGS, following the procedures described by Hou et al. [33]. Spot sizes were ~25 μm and data were calibrated by the M127 reference zircon (U: 923 ppm; Th: 439 ppm; Th/U: 0.475) [34]. The standard zircon was analyzed first and then after every five unknowns. The GJ-1 zircon with an age of 599.8± 1.7 Ma (2σ) [35] was used as a standard. Data process was carried out using the ICPMSDataCal programs [36], and for the ^{206}Pb/^{204}Pb values of most analysis spots larger than 1000, measured ^{204}Pb was not applied for the common lead correction, thus those analysis with unusual high ^{204}Pb are deleted due to the influence of common lead in inclusions. The analytical data are summarized in Table 1, and graphically

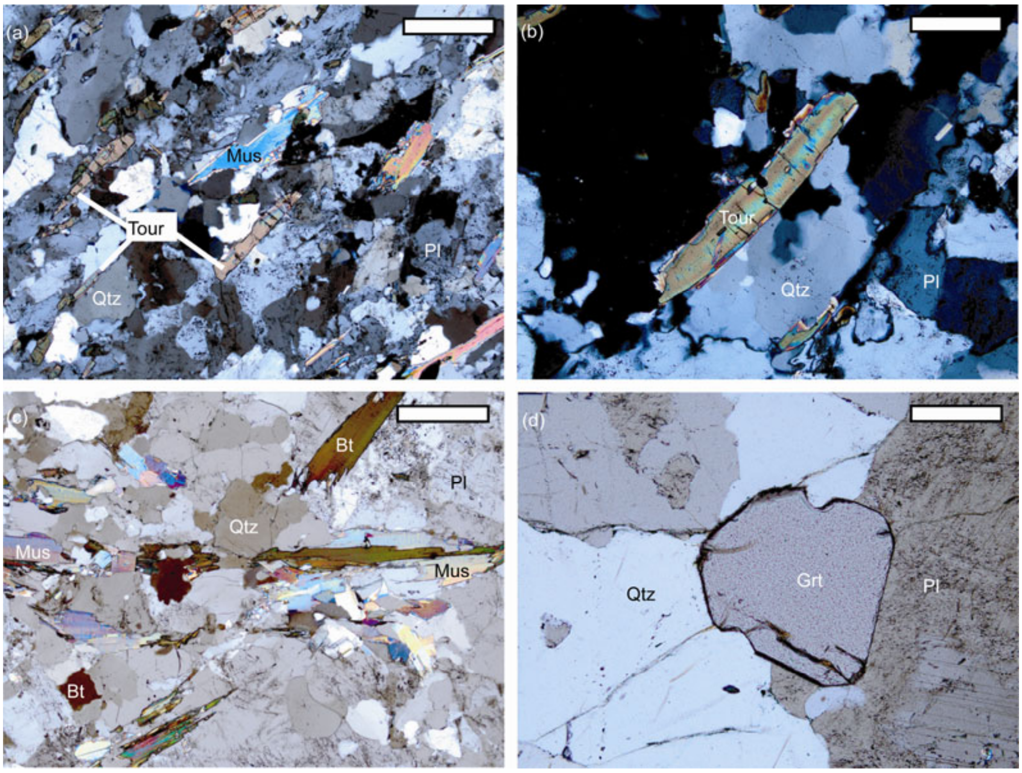

Figure 2 Photomicrographs showing the texture and mineral assemblage of three types of leucogranite in the Paiku area. (a) and (b) tourmaline leucogranite T0659-03 consists of quartz, plagioclase, muscovite and euhedral compositionally zoned tourmaline; (c) two-mica granite T0659-11 consists of quartz, plagioclase, muscovite and biotite; (d) garnet-bearing leucogranite T0659-09 consists of quartz, plagioclase, muscovite and garnet. Except for (a) and (c) with a 500-μm-long scale bar, the others are 250 μm long. Bt, biotite; Grt, garnet; Mus, muscovite; Pl, plagioclase; Qtz, quartz; Tour, tourmaline.

presented on concordia diagrams with 1σ error. The ages are weighted means with 2σ errors calculated using Isoplot at 95% confidence levels [37].

2.2 Zircon Hf isotope analysis

Zircon Hf isotope analysis was carried out in-situ using a Newwave UP213 laser-ablation microprobe, attached to a Neptune multi-collector ICP-MS at Institute of Mineral Resources, CAGS, Beijing. Instrumental conditions and data acquisition were comprehensively described by Hou et al. [38]. A stationary spot was used for the present analyses, with a beam diameter of 40 μm. The analyses were performed on the same zircon domains where the U-Pb dating had been conducted or on the zircons with similar texture. Helium was used as carrier gas to transport the ablated sample from the laser-ablation cell to the ICP-MS torch via a mixing chamber mixed with Argon. In order to correct the isobaric interferences of ^{176}Lu and ^{176}Yb on ^{176}Hf, ^{176}Lu/^{175}Lu=0.02658 and ^{176}Yb/^{173}Yb=0.796218 ratios were applied [39]. For instrumental mass bias correction, Yb isotope ratios were normalized to ^{172}Yb/^{173}Yb of 1.35274 [39] and Hf isotope ratios to ^{179}Hf/^{177}Hf of 0.7325 using an exponential law. The mass bias behavior of Lu was assumed to follow that of Yb, mass bias correction protocols details was described as Wu et al. [40] and Hou et al. [38]. Zircon GJ-1 and Plesovice were used as the reference standards during our routine analyses, with a weighted mean ^{176}Hf/^{177}Hf ratio of 0.282007±0.000007 (2σ, n=36) and 0.282476±0.000004 (2σ, n=27), respectively. It is not distinguishable from a weighted mean ^{176}Hf/^{177}Hf ratio of 0.282000±0.000005 (2σ) and 0.282482±0.000008 (2σ) using a solution analysis method by Morel et al. [41] and Sláma et al. [42], respectively. To calculate the initial Hf isotope compositions, age of ~28 Ma and ~20 Ma were assigned for the Paiku tourmaline leucogranites and two-mica granites based on their U/Pb zircon age, respectively. Analytical results are listed in Table 2.

2.3 Major and trace element analysis

Whole rock powders for 12 whole-rock samples were prepared by using a tungsten carbide shatter box. Bulk rock major, trace and rare earth element concentrations were obtained by X-ray fluorescence (XRF) and inductively coupled plasma mass spectrometry (ICP-MS) at the National Research Center for Geoanalysis, CAGS, Beijing. Major elements were analyzed by the XRF method with analytical uncertainties <5%. Trace and rare earth elements were analyzed by ICP-MS. REE were separated using cation-exchange techniques. Analytical uncertainties are 10% for elements with abundances <10 ppm, and around 5% for those >10 ppm. Analytical results are listed in Table 3.

Table 1 U-Pb isotopic data for the tourmaline leucogranite T0659-A and the two-mica granite T0659-B from the Paiku area

Spot	Domain	Pb (ppm)	Th (ppm)	U (ppm)	Th/U	$^{207}Pb/^{206}Pb$	1σ (%)	$^{207}Pb/^{235}U$	1σ (%)	$^{206}Pb/^{238}U$	1σ (%)	Err corr	$^{207}Pb/^{235}U$ age (Ma)		$^{206}Pb/^{238}U$ age (Ma)		Discordance (%)
T0659-A: tourmaline leucogranite																	
T0659-A-1	core	16.74	25	814	0.03	0.0534	0.0002	0.3480	0.0350	0.0472	0.0046	0.9653	303.19	26.37	297.32	28.21	98
T0659-A-2	rim	422.7	553	10184	0.05	0.0478	0.0003	0.0295	0.0009	0.0045	0.0001	0.9656	29.50	0.93	28.73	0.88	97
T0659-A-3	core	907.88	33	345	0.10	0.0565	0.0003	0.4614	0.0079	0.0592	0.0009	0.8748	385.21	5.47	370.58	5.38	96
T0659-A-4	core	4734.51	60	83	0.72	0.0729	0.0003	1.6461	0.0175	0.1641	0.0017	0.9928	988.07	6.70	979.37	9.57	99
T0659-A-5	mantle	863.68	23	285	0.08	0.0565	0.0004	0.5894	0.0106	0.0757	0.0013	0.9617	470.46	6.80	470.42	7.88	99
T0659-A-6	rim	9.36	29	980	0.03	0.0539	0.0007	0.1406	0.0066	0.0189	0.0009	1.0639	133.60	5.90	120.93	6.01	90
T0659-A-7	core	384.53	10	457	0.02	0.0568	0.0002	0.5990	0.0061	0.0765	0.0008	0.9671	476.60	3.86	475.19	4.50	99
T0659-A-8	rim	2062.68	152	10460	0.01	0.0498	0.0005	0.0314	0.0008	0.0046	0.0001	0.7995	31.36	0.82	29.34	0.62	93
T0659-A-9	core	4732.45	115	344	0.34	0.057	0.0003	0.5961	0.0123	0.0759	0.0015	0.9337	474.75	7.80	471.52	8.73	99
T0659-A-10	mantle	162.26	69	2488	0.03	0.0483	0.0003	0.0347	0.0003	0.0052	0	0.7937	34.61	0.30	33.47	0.24	96
T0659-A-11	rim	1.33	44	751	0.06	0.0468	0.0009	0.0275	0.0007	0.0043	0.0001	0.6681	27.54	0.66	27.44	0.45	99
T0659-A-12	core	2.62	11	509	0.02	0.0496	0.0012	0.0722	0.0028	0.0106	0.0004	0.8743	70.80	2.63	67.8	2.27	95
T0659-A-13	core	12.79	5	456	0.01	0.0567	0.0002	0.4901	0.0056	0.0627	0.0007	0.9404	404.98	3.82	391.88	4.09	96
T0659-A-14	mantle	0.56	5	209	0.03	0.0615	0.0032	0.0433	0.0023	0.0052	0.0002	0.8068	43.07	2.26	33.14	1.43	73
T0659-A-15	core	2028.75	34	35	0.96	0.0719	0.0005	1.6186	0.0196	0.1634	0.0018	0.9291	977.44	7.60	975.83	10.19	99
T0659-A-16	rim	204.81	51	3306	0.02	0.0478	0.0003	0.0294	0.0003	0.0045	0	0.9139	29.38	0.32	28.65	0.29	97
T0659-A-17	core	1907.62	55	131	0.42	0.0722	0.0010	1.1432	0.0489	0.1149	0.0047	0.9471	774.03	23.16	701.16	26.90	90
T0659-A-18	mantle	633.6	248	2201	0.11	0.0476	0.0003	0.0343	0.0006	0.0052	0.0001	0.9311	34.21	0.58	33.56	0.54	98
T0659-A-19	rim	3.99	53	2167	0.02	0.048	0.0004	0.0292	0.0004	0.0044	0.0001	0.9061	29.18	0.40	28.35	0.36	97
T0659-A-20	rim	1954.27	427	6874	0.06	0.0726	0.0012	0.0448	0.0017	0.0045	0.0001	0.7821	44.51	1.65	28.75	0.85	56
T0659-A-21	rim	537.89	11	326	0.03	0.0654	0.0031	0.0311	0.0015	0.0035	0.0002	1.1334	31.14	1.45	22.37	1.19	67
T0659-A-22	rim	735.39	261	3570	0.07	0.0482	0.0008	0.0281	0.0006	0.0042	0	0.2004	28.18	0.56	27.25	0.11	96
T0659-A-23	mantle	1252.45	548	1991	0.28	0.084	0.0007	0.0553	0.0017	0.0048	0.0002	1.0245	54.62	1.66	30.73	0.98	44
T0659-A-24	rim	71.91	39	2247	0.02	0.0476	0.0008	0.0288	0.0010	0.0044	0.0001	0.7885	28.85	0.96	28.23	0.75	97
T0659-A-25	mantle	5230.49	319	3723	0.09	0.1613	0.0012	0.1224	0.0017	0.0055	0.0001	0.7797	117.22	1.56	35.33	0.39	–8
T0659-A-26	mantle	155.93	4	94	0.05	0.0483	0.0049	0.0353	0.0036	0.0053	0.0001	0.2723	35.25	3.50	34.16	0.94	96
T0659-A-27	rim	260.14	92	1888	0.05	0.0505	0.0008	0.0303	0.0008	0.0044	0.0001	0.9816	30.26	0.80	28.02	0.73	92
T0659-A-28	mantle	2.42	13	1037	0.01	0.0491	0.0008	0.0370	0.0010	0.0055	0.0001	0.7834	36.86	0.96	35.08	0.73	95
T0659-A-29	rim	414.41	60	782	0.08	0.0466	0.0007	0.0279	0.0005	0.0044	0.0001	0.6811	27.96	0.51	27.99	0.35	99
T0659-A-30	mantle	184.56	47	2116	0.02	0.0637	0.0017	0.0411	0.0020	0.0047	0.0002	0.8668	40.88	1.94	30.13	1.26	69

(*To be continued on the next page*)

(Continued)

Spot	Domain	Pb (ppm)	Th (ppm)	U (ppm)	Th/U	$^{207}Pb/^{206}Pb$	1σ (%)	$^{207}Pb/^{235}U$	1σ (%)	$^{206}Pb/^{238}U$	1σ (%)	Err corr	$^{207}Pb/^{235}U$ age (Ma)		$^{206}Pb/^{238}U$ age (Ma)		Discordance (%)
T0659-A-31	core	1620.58	97	346	0.28	0.0572	0.0003	0.6009	0.0078	0.0761	0.001	0.956	477.81	4.98	473.09	5.69	99
T0659-A-32	core	10708.68	153	93	1.65	0.1151	0.0004	5.5138	0.0641	0.3475	0.0038	0.9338	1902.75	9.99	1922.44	18.05	98
T0659-A-33	mantle	1840.86	59	1275	0.05	0.1605	0.0042	0.1397	0.0029	0.0063	0.0001	0.7783	132.82	2.57	40.6	0.65	–7
T0659-A-34	mantle	4333.93	62	2880	0.02	0.1527	0.0043	0.1085	0.0032	0.0051	0	0.1299	104.58	2.96	32.96	0.13	–5
T0659-A-35	rim	7.24	49	3108	0.02	0.0497	0.0004	0.03	0.0003	0.0044	0	0.8909	29.98	0.27	28.14	0.23	93
T0659-A-36	core	1517.22	57	419	0.14	0.0564	0.0002	0.4665	0.0033	0.06	0.0004	0.8882	388.75	2.27	375.53	2.28	96
T0659-A-37	core	3156.54	633	825	0.77	0.0589	0.0005	0.3791	0.0039	0.0466	0.0002	0.4116	326.38	2.84	293.76	1.2	89
T0659-A-38	core	1327.27	43	191	0.23	0.0621	0.0003	0.8319	0.0051	0.0972	0.0005	0.7849	614.65	2.84	598.13	2.76	97
T0659-A-39	core	3830.83	89	85	1.06	0.0681	0.0004	1.2693	0.0089	0.1351	0.0006	0.6651	832.08	3.99	817.08	3.59	98
T0659-A-40	core	3690.15	138	127	1.08	0.0582	0.0004	0.6317	0.0049	0.0787	0.0004	0.59	497.17	3.04	488.18	2.14	98
T0659-B: two-mica granite																	
T0659-B-1	core	500.82	122	833	0.15	0.0576	0.0001	0.6126	0.0057	0.0771	0.0007	0.9653	485.21	3.62	478.98	4.18	98
T0659-B-2	mantle	54.94	61	2991	0.02	0.0477	0.0003	0.0227	0.0003	0.0035	0	0.9117	22.82	0.31	22.26	0.28	97
T0659-B-3	core	2403.85	329	603	0.55	0.072	0.0003	1.5072	0.0105	0.1519	0.0006	0.5255	933.32	4.27	911.51	3.12	97
T0659-B-4	mantle	4.96	21	323	0.06	0.0479	0.0022	0.0198	0.0009	0.003	0.0001	0.7547	19.88	0.88	19.44	0.65	97
T0659-B-5	mantle	1.24	49	743	0.07	0.048	0.0008	0.0264	0.0006	0.004	0.0001	0.6	26.44	0.58	25.63	0.34	96
T0659-B-6	rim	257.12	53	1954	0.03	0.1227	0.002	0.0568	0.0015	0.0033	0.0001	0.6797	56.05	1.44	21.53	0.39	11
T0659-B-7	core	66.12	14	170	0.08	0.0569	0.0003	0.6072	0.0078	0.0774	0.0009	0.8839	481.82	4.91	480.86	5.24	99
T0659-B-8	mantle	25.95	2	363	0.01	0.0468	0.0015	0.0231	0.0007	0.0036	0.0001	0.4978	23.2	0.7	23.13	0.35	99
T0659-B-9	core	964.96	335	1724	0.19	0.0661	0.0011	0.666	0.0242	0.073	0.002	0.7689	518.28	14.74	454.2	12.24	86
T0659-B-10	mantle	2.62	0	217	0	0.0852	0.0042	0.0602	0.0051	0.0051	0.0003	0.6329	59.4	4.89	32.85	1.76	42
T0659-B-11	core	185.6	67	212	0.32	0.0593	0.0004	0.4201	0.0082	0.0514	0.0009	0.8903	356.14	5.85	322.85	5.46	90
T0659-B-12	mantle	59.69	439	639	0.69	0.0507	0.002	0.022	0.0012	0.0032	0.0001	0.8014	22.14	1.15	20.33	0.86	91
T0659-B-13	mantle	10.93	80	575	0.14	0.0489	0.0016	0.0213	0.0008	0.0032	0	0.4372	21.42	0.77	20.33	0.32	94
T0659-B-14	core	272.63	93	99	0.94	0.0566	0.0006	0.4924	0.0079	0.0632	0.0009	0.8903	406.57	5.37	395.03	5.47	97
T0659-B-15	core	130.26	66	172	0.38	0.0582	0.0003	0.6504	0.0067	0.081	0.0007	0.8763	508.71	4.1	502.02	4.34	98
T0659-B-16	core	240.9	88	795	0.11	0.057	0.0002	0.4735	0.0057	0.0603	0.0007	0.959	393.59	3.96	377.22	4.27	95
T0659-B-17	core	78.5	103	702	0.15	0.0571	0.0006	0.1161	0.003	0.0147	0.0004	0.9276	111.5	2.75	94.28	2.26	83
T0659-B-18	core	138.33	44	148	0.3	0.057	0.0004	0.6099	0.0057	0.0777	0.0006	0.8396	483.49	3.57	482.18	3.62	99
T0659-B-19	mantle	51.04	28	110	0.26	0.0512	0.004	0.021	0.0016	0.003	0	0.2107	21.13	1.6	19.22	0.31	90
T0659-B-20	rim	5.63	3	186	0.02	0.0573	0.0006	0.5239	0.0102	0.0665	0.0012	0.9065	427.77	6.81	414.74	7.1	96
T0659-B-21	core	382.02	124	478	0.26	0.0577	0.0002	0.6163	0.0074	0.0775	0.0009	0.9698	487.54	4.65	481.37	5.4	98
T0659-B-22	core	650.23	207	1086	0.19	0.0592	0.0002	0.6347	0.0069	0.0778	0.0008	0.9654	499.01	4.28	482.98	4.88	96

Table 2 Hf isotope compositions of the tourmaline leucogranite T0659-A and the two-mica granite T0659-B from the Paiku area

Spot	Domain	U-Pb age (Ma)	$^{176}Yb/^{177}Hf$	±2σ	$^{176}Lu/^{177}Hf$	±2σ	$^{176}Hf/^{177}Hf$	±2σ	$^{176}Hf/^{177}Hf$ (t)	ε_{Hf} (t)	±2σ	T_{DM1} (Ma)	T_{DM2} (Ma)	f (Lu/Hf)
T0659-A: tourmaline leucogranite														
T0659A-01	rim	28.7	0.07073	0.00074	0.00161	0.00001	0.2826	0.00002	0.28260	–5.6	0.6	942	1466	–0.95166
T0659A-02	core	370.6	0.05667	0.00157	0.00132	0.00003	0.28236	0.00002	0.28236	–14.1	0.6	1275	2003	–0.96034
T0659A-03	core	979.4	0.04017	0.00118	0.00086	0.00002	0.2822	0.00002	0.28220	–19.5	0.8	1472	2345	–0.97419
T0659A-04	rim	33.5	0.10394	0.00076	0.00282	0.00002	0.28268	0.00002	0.28267	–2.8	0.6	857	1289	–0.91510
T0659A-05	core		0.11296	0.00033	0.00245	0.00001	0.28229	0.00002	0.28229	–16.4	0.7	1410	2151	–0.92622
T0659A-06	core		0.03312	0.00017	0.00074	0.00001	0.28206	0.00002	0.28206	–24.5	0.7	1662	2658	–0.97761
T0659A-07	core	475.2	0.09065	0.00036	0.00202	0.00001	0.28239	0.00002	0.28239	–12.9	0.6	1248	1925	–0.93918
T0659A-08	rim	27.4	0.03608	0.00039	0.00077	0.00001	0.28244	0.00002	0.28244	–11.2	0.8	1142	1820	–0.97691
T0659A-09	core	975.8	0.03088	0.00011	0.00069	0.00000	0.28218	0.00002	0.28218	–20.4	0.8	1502	2404	–0.97926
T0659A-10	rim	34.2	0.01548	0.00026	0.0003	0.00001	0.28252	0.00002	0.28252	–8.3	0.7	1017	1637	–0.99088
T0659A-11	rim	33.6	0.04671	0.00231	0.00107	0.00005	0.28244	0.00002	0.28244	–11.1	0.6	1149	1816	–0.96771
T0659A-12	rim	28.7	0.11797	0.00132	0.00255	0.00001	0.28249	0.00002	0.28249	–9.5	0.7	1126	1711	–0.92322
T0659A-13	rim	30.1	0.09534	0.00153	0.00218	0.00005	0.28249	0.00003	0.28249	–9.3	0.9	1108	1700	–0.93438
T0659A-14	rim	35.1	0.04408	0.00082	0.00119	0.00002	0.28258	0.00002	0.28258	–6.2	0.5	957	1505	–0.96427
T0659A-15	rim		0.03782	0.00019	0.001	0.00000	0.28253	0.00001	0.28253	–7.8	0.4	1016	1607	–0.96978
T0659A-16	rim	33.0	0.06181	0.00037	0.00194	0.00002	0.28256	0.00002	0.28256	–6.8	0.5	998	1540	–0.94143
T0659A-17	rim		0.08151	0.00025	0.00196	0.00000	0.28237	0.00002	0.28237	–13.8	0.7	1283	1982	–0.94083
T0659A-18	core	297.3	0.04471	0.00131	0.00097	0.00003	0.28227	0.00002	0.28227	–17.0	0.6	1379	2189	–0.97083
T0659A-19	core	475.2	0.07244	0.00104	0.00169	0.00003	0.2824	0.00002	0.28240	–12.6	0.6	1229	1912	–0.94924
T0659A-20	core	471.5	0.1087	0.0014	0.00256	0.00004	0.28246	0.00002	0.28246	–10.5	0.6	1169	1776	–0.92290
T0659A-21	rim		0.09133	0.00042	0.00205	0.00002	0.28255	0.00002	0.28255	–7.1	0.6	1016	1563	–0.93812
T0659-B: two-mica granite														
T0659B-01	core	478.9	0.13232	0.00037	0.00293	0.00001	0.2823	0.00002	0.28229	–16.4	0.7	1420	2143	–0.91187
T0659B-02	core		0.11904	0.00416	0.00282	0.00008	0.28247	0.00002	0.28247	–10.1	0.6	1156	1747	–0.91504
T0659B-03	core		0.03557	0.00011	0.0008	0.00000	0.28179	0.00002	0.28179	–34.3	0.6	2041	3268	–0.97598
T0659B-04	core		0.08763	0.00068	0.00204	0.00002	0.28223	0.00002	0.28223	–18.7	0.7	1481	2290	–0.93863
T0659B-06	core		0.01638	0.0002	0.00032	0.00000	0.28245	0.00001	0.28245	–11.1	0.5	1120	1810	–0.99033
T0659B-07	core	480.9	0.10468	0.00101	0.00234	0.00001	0.2822	0.00002	0.28220	–19.8	0.7	1537	2358	–0.92966
T0659B-08	rim	21.5	0.06787	0.00071	0.00164	0.00001	0.28234	0.00002	0.28233	–15.0	0.5	1315	2055	–0.95075
T0659B-09	rim	22.3	0.13098	0.00155	0.00262	0.00002	0.2825	0.00002	0.28249	–9.3	0.6	1116	1696	–0.92104
T0659B-10	rim	19.4	0.02578	0.00036	0.00059	0.00001	0.28237	0.00002	0.28237	–13.9	0.6	1237	1986	–0.98212
T0659B-11	core		0.04118	0.00039	0.00089	0.00001	0.28212	0.00002	0.28212	–22.6	0.7	1589	2536	–0.97328
T0659B-12	core		0.02249	0.0003	0.00051	0.00000	0.28201	0.00002	0.28201	–26.7	0.6	1731	2790	–0.98471
T0659B-13	core		0.05531	0.00038	0.00127	0.00000	0.28227	0.00002	0.28227	–17.4	0.6	1397	2204	–0.96161
T0659B-14	core		0.07186	0.00152	0.00147	0.00002	0.28233	0.00002	0.28233	–15.3	0.8	1323	2077	–0.95567
T0659B-15	rim	19.2	0.05037	0.00071	0.00114	0.00002	0.28234	0.00002	0.28234	–14.9	0.6	1296	2051	–0.96554
T0659B-16	core	322.8	0.08715	0.00079	0.00184	0.00002	0.28198	0.00003	0.28198	–27.5	0.9	1824	2839	–0.94452
T0659B-17	rim	32.8	0.03427	0.00017	0.00076	0.00000	0.28238	0.00002	0.28238	–13.3	0.7	1219	1949	–0.97718
T0659B-18	rim	20.3	0.0573	0.00075	0.00135	0.00002	0.28241	0.00002	0.28240	–12.5	0.7	1207	1899	–0.95943
T0659B-19	core		0.09956	0.0012	0.00212	0.00001	0.28218	0.00003	0.28218	–20.5	0.9	1555	2401	–0.93628
T0659B-21	rim	20.3	0.10764	0.00338	0.00311	0.00011	0.28243	0.00002	0.28243	–11.6	0.7	1226	1839	–0.90636
T0659B-22	core	482.2	0.03688	0.00041	0.00061	0.00001	0.28238	0.00002	0.28238	–13.5	0.8	1222	1961	–0.98169
T0659B-23	rim	19.2	0.03774	0.00053	0.00081	0.00001	0.28246	0.00002	0.28246	–10.8	0.8	1120	1787	–0.97559
T0659B-24	core	481.4	0.07139	0.00103	0.00161	0.00002	0.28237	0.00002	0.28237	–13.8	0.7	1267	1981	–0.95150
T0659B-25	core		0.06652	0.00027	0.00149	0.00000	0.28197	0.00002	0.28197	–28.0	0.7	1830	2875	–0.95514

Table 3 Major and trace element compositions of tourmaline leucogranites, garnet-bearing leucogranites and two-mica granites from the Paiku area

Rock-type	Tourmaline leucogranite					Garnet-bearing leucogranite			Two-mica granite			
Sample No.	T0659-1	T0659-3	T0659-4	T0659-5	T0659-6	T0659-7	T0659-8	T0659-9	T0659-11	T0659-12	T0659-13	T0659-14
Major elements (wt.%)												
SiO_2	72.51	72.54	72.96	73.22	72.92	73.59	74.24	75.01	73.68	73.34	73.51	73.91
TiO_2	0.09	0.08	0.09	0.08	0.09	0.04	0.02	0.02	0.07	0.09	0.08	0.06
Al_2O_3	14.94	14.95	14.9	14.96	14.81	14.62	14.6	14.25	14.49	14.42	14.5	14.8
FeO	0.32	0.31	0.27	0.18	0.18	0.56	0.38	0.38	0.52	0.41	0.52	0.57
Fe_2O_3	0.44	0.45	0.44	0.64	0.57	0	0	0	0.29	0.41	0.43	0.2
MnO	0.01	0.01	0.01	0.01	0.01	0.02	0.01	0.02	0.02	0.01	0.02	0.01
MgO	0.2	0.22	0.21	0.17	0.2	0.18	0.35	0.23	0.27	0.37	0.16	0.13
CaO	0.72	0.7	0.7	0.73	0.72	1.02	1.16	1.02	1.02	1.12	0.92	0.98
Na_2O	3.98	4.12	4.54	3.82	4.08	3.99	4.23	4.06	4.06	4.14	3.34	3.96
K_2O	5.38	5.31	4.89	5.39	5.25	4.5	4.38	4.18	4.38	4.27	4.93	4.52
P_2O_5	0.21	0.21	0.19	0.2	0.2	0.09	0.06	0.04	0.06	0.05	0.07	0.05
LOI	0.7	0.61	0.77	0.72	0.66	0.65	0.43	0.41	0.73	0.66	0.82	0.86
Total	99.5	99.51	99.97	100.12	99.69	99.26	99.86	99.62	99.59	99.29	99.3	100.05
Trace elements (ppm)												
Sc	2.92	2.8	2.44	2.63	2.17	1.47	2.03	1.93	1.5	2.32	2.07	1.45
V	1.55	2.42	2.03	2.25	1.72	1.54	0.77	0.27	3.83	7.21	3.46	3.21
Cr	15.9	7.79	33.9	4.12	16.2	0.8	1.24	0.81	34.3	11	57.6	11.6
Ni	9.14	3.41	18	1.8	7.67	0.96	1.06	0.89	15.2	4.5	29.6	5.58
Co	0.74	0.8	0.97	0.79	0.77	0.6	0.33	0.4	1.16	1.25	1.39	0.9
B	1089	1033	1063	1088	1053	13.1	22.6	12.7	15.2	36	14.5	16
Rb	366	369	338	350	348	302	309	311	327	292	349	333
Sr	38.2	38.9	38.1	33.5	37.3	72.6	55.6	40.2	70.9	119	75.6	63.5
Y	8.89	8.6	7.32	8	8.56	16.1	20.1	18.7	12	8.76	11.7	9.58
Zr	32.5	32.2	34.8	31.3	32.4	23.6	59.8	42.5	34.1	25.6	32.4	23.8
Nb	9.82	8.3	8.67	9.59	11.7	6.77	4.62	7.14	8.29	6	8.45	7.84
Cs	9.29	9.43	7.59	9.45	8.89	6.66	7.56	8.94	7.77	5.52	6.65	7.69
Ba	144	165	157	131	135	88.2	48.8	33.8	165	289	176	153
Hf	1.7	1.7	1.8	1.6	1.7	1.03	2.51	1.8	1.9	1.3	1.6	1.4
Ta	2.4	2	2.1	2.5	3	1.24	0.66	0.99	2.1	1.7	2.2	1.7
Pb	47.6	53.6	46.7	45.8	45	47.5	49.6	50.6	44.6	50.8	51.2	45.6
Th	3.55	2.93	3.24	3.17	3.64	3	2.84	3.75	4.4	3.49	4.44	4.35
U	2.35	2.48	2.85	2.52	2.1	1.74	2.7	4.27	1.75	1.61	1.81	1.49
Rare earth elements (ppm)												
La	5.34	4.46	4.69	4.8	5.53	5.19	4.18	5.57	8.16	6.48	7.32	7.96
Ce	10.1	8.85	9.34	8.8	10.4	9.55	7.53	10.8	17.6	13.4	15.4	16.5
Pr	1.16	0.97	0.99	1.01	1.18	1.25	0.99	1.29	1.99	1.52	1.72	1.94

(*To be continued on the next page*)

(*Continued*)

Rock-type	Tourmaline leucogranite					Garnet-bearing leucogranite			Two-mica granite			
Sample No.	T0659-1	T0659-3	T0659-4	T0659-5	T0659-6	T0659-7	T0659-8	T0659-9	T0659-11	T0659-12	T0659-13	T0659-14
Nd	4.04	3.36	3.37	3.4	4.12	4.57	3.73	4.69	7.29	5.42	6.16	6.85
Sm	1.03	0.94	0.98	1.02	1.19	1.59	1.29	1.4	2.11	1.5	1.89	1.9
Eu	0.26	0.24	0.23	0.21	0.23	0.37	0.22	0.14	0.39	0.61	0.39	0.37
Gd	1.25	1.16	1.11	1.08	1.33	1.95	1.81	1.76	2.32	1.51	2.06	2.01
Tb	0.25	0.23	0.22	0.22	0.24	0.42	0.4	0.38	0.38	0.28	0.34	0.32
Dy	1.59	1.51	1.37	1.42	1.58	2.62	2.91	2.73	2.28	1.6	2.05	1.81
Ho	0.3	0.28	0.24	0.26	0.29	0.51	0.65	0.59	0.4	0.27	0.4	0.32
Er	0.81	0.73	0.68	0.72	0.78	1.49	2.14	1.8	1.05	0.81	1.14	0.88
Tm	0.11	0.1	0.09	0.1	0.11	0.24	0.35	0.29	0.17	0.12	0.16	0.13
Yb	0.63	0.63	0.57	0.62	0.67	1.68	2.48	1.97	1	0.9	1.1	0.88
Lu	0.09	0.09	0.08	0.08	0.09	0.23	0.41	0.28	0.1	0.1	0.2	0.12
ΣREE	26.96	23.55	23.96	23.74	27.74	31.66	29.09	33.69	45.32	34.49	40.32	41.99
Na_2O/K_2O	0.74	0.78	0.93	0.71	0.78	0.89	0.97	0.97	0.93	0.97	0.68	0.88
A/CNK	1.09	1.08	1.06	1.11	1.08	1.1	1.06	1.09	1.09	1.07	1.16	1.12
Nb/Ta	4.14	4.11	4.09	3.79	3.86	5.46	7	7.21	4.02	3.45	3.79	4.64
Zr/Hf	19.35	19.05	19.44	19.69	19.4	22.91	23.82	23.61	17.58	19.54	20	17
Eu/Eu*	0.71	0.71	0.68	0.62	0.57	0.65	0.45	0.28	0.55	1.25	0.61	0.59
Ce/Ce*	0.96	1.00	1.02	0.94	0.96	0.88	0.87	0.95	1.03	1.01	1.02	0.99
$(La/Yb)_N$	5.96	4.98	5.79	5.45	5.81	2.17	1.19	1.99	5.52	5.36	4.56	6.36
$(La/Gd)_N$	3.6	3.24	3.56	3.75	3.51	2.24	1.95	2.67	2.97	3.62	3	3.34
$(Gd/Yb)_N$	1.66	1.54	1.62	1.45	1.66	0.97	0.61	0.75	1.86	1.48	1.52	1.91

Table 4 Sr and Nd isotope compositions of tourmaline leucogranites and two-mica granites from the Paiku area

Sample	Rb (ppm)	Sr (ppm)	$^{87}Rb/^{86}Sr$	$^{87}Sr/^{86}Sr$	$\pm 2\sigma$	Sm (ppm)	Nd (ppm)	$^{147}Sm/^{144}Nd$	$^{143}Nd/^{144}Nd$	$\pm 2\sigma$	$^{87}Sr/^{86}Sr\ (t)$	$\varepsilon_{Nd}\ (t)$
Tourmaline leucogranite												
T0659-3	369.0	38.9	27.414	0.763382	13	3.36	0.94	0.169	0.511956	5	0.7525	−13.2
T0659-4	338.0	38.1	25.638	0.761717	13	3.37	0.98	0.176	0.511968	5	0.7516	−13.0
T0659-6	348.0	37.3	26.963	0.760200	16	4.12	1.19	0.175	0.511952	13	0.7495	−13.3
Two-mica granite												
T0659-11	327.0	70.9	13.329	0.732263	14	7.29	2.11	0.175	0.511946	11	0.7285	−13.4
T0659-12	292.0	119.0	7.091	0.747446	16	5.42	1.50	0.167	0.511946	10	0.7454	−13.4
T0659-13	349.0	75.6	13.341	0.747321	17	6.16	1.89	0.186	0.511925	8	0.7435	−13.9
T0659-14	333.0	63.5	15.155	0.748351	21	6.85	1.90	0.168	0.511926	7	0.7441	−13.8

2.4 Sr and Nd isotope analysis

Rb-Sr and Sm-Nd isotope analyses were performed in the Laboratory for Isotope Analysis, Institute of Geology, CAGS. The Sr isotope compositions and concentrations of Rb, Sr, Sm, and Nd were measured by isotope dilution on a Finnigan MAT-262 mass spectrometer. Nd isotope compositions were acquired by a Nu Plasam HR MC-ICP-MS (Nu Instruments). The Nd and Sr measurements were corrected for mass fractionation by normalization to $^{146}Nd/^{142}Nd$=0.7219, and $^{86}Sr/^{88}Sr$=0.1194. External precisions during this period of measurement for Sr and Nd isotopic compositions are ±0.000010 (n=18) and ±0.000011 (n=18), respectively. $^{87}Sr/^{86}Sr$ for the NBS987 standard is 0.710247±12 (2σ) and $^{143}Nd/^{144}Nd$ for JMC Nd standard is 0.511127±12 (2σ). At ~28 Ma and ~20 Ma were assigned to calculate the initial Sr and Nd isotope compositions for the Paiku tourmaline leucogranites and two-mica granites based on their U/Pb zircon age. Analytical results are listed in Table 4.

3 Date and results

3.1 The U/Pb zircon age of leucogranites

Sample T0659-A is a representative sample of tourmaline leucogranite that consists of quartz, plagioclase, muscovite, tourmaline, and accessory zircon, apatite, and monazite. Most of zircon grains in this sample are euhedral to subhedral, long prismatic, 100–150 μm long with aspect ratios commonly of 2.5. These zircons show a similar core-mantle-rim texture both in CL and in BSE images (Figure 3(a)–(d)). The cores are either homogeneous (Figure 3(a), (b)) or weak oscillatory zoning (Figure 3(c), (d)). The mantles are characterized by either weak oscillatory growth zoning or gray homogeneous (Figure 3(a)–(d)), which implies that the source for this granite had experienced simultaneous metamorphism and partial melting. The zircon rims have very high U concentration (>2000 ppm), and due to radioactive decay of U, a large portion of zircon crystals experienced intensive destruction and recrystallization and show sponge-like textures. However, many zircon grains still preserve rims with typical oscillatory growth zoning, characteristics of magmatic zircon. In addition, the outermost part of a few of zircon grains also contain white narrow rims about 5–10 μm thick (Figure 3(a)–(c)), which could be due to hydrothermal or metamorphic events postdated the crystallization.

To constrain more precisely on the crystallization age and possible hydrothermal event of the Paiku tourmaline leucogranite, U/Pb analyses were focused on different zircon domains in sample T0659-A. The cores are characterized by (1) relatively low but wide variations in U (35–814 ppm) and Th (5–153 ppm), respectively, which results in great variations in Th/U ratio from 0.02 to 1.65; (2) relatively wide range in $^{206}Pb/^{238}U$ age from 297.3 Ma to 1922.4 Ma (Table 1); (3) a cluster of grains with concordant $^{206}Pb/^{238}U$ ages of 470.4–488.2 Ma with a weighted mean age of 483.3 Ma; and (4) another cluster at ~851.0 Ma, the others are discordant due to various degrees of Pb loss.

Many analyses performed on mantle and a few on rim domains yielded discordant ages with concordance down to −8%, therefore we choose points with concordance higher than 95% to calculate meaningful ages. Analyses on the mantles show that they have a relatively wide range of U and Th concentrations from 94 to 2488 ppm, and from 4 to 248 ppm, respectively, and Th/U from 0.01 to 0.11. The mantles yield $^{206}Pb/^{238}U$ ages from 33.5±0.2 Ma to 35.1±0.7 Ma (Figure 3(e)) with a cluster around 33.6 Ma. The mean age of 4 points is 33.6±0.6 Ma (MSWD=1.6). The mantle domains either with weak oscillatory growth zoning or with

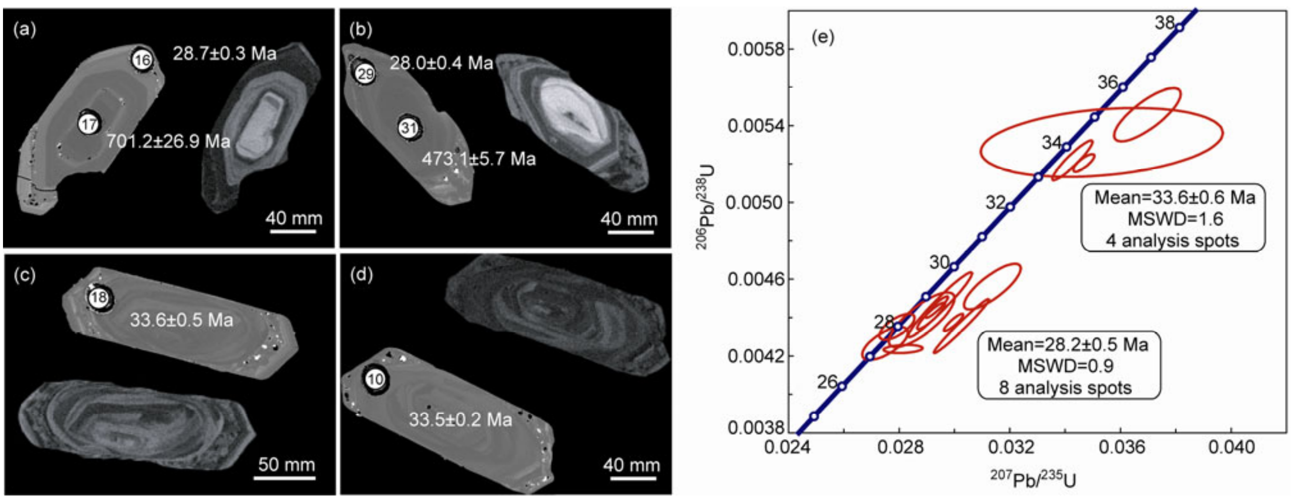

Figure 3 Cathodoluminescence (CL) and Backscatter images (BSE) showing the texture, spot, and respective age of LA-MC-ICP-MS zircon U/Pb dating (a)–(d) and U/Pb concordia diagram (e) for the tourmaline leucogranite T0659-A.

gray homogeneous texture yield similar $^{206}Pb/^{238}U$ ages, therefore we interpret this age as the timing of high-grade metamorphism and simultaneous parting melting experienced in the source rocks. Except for few zircon grains, the rims with well-developed oscillatory zoning commonly yielded $^{206}Pb/^{238}U$ ages with concordance higher than 95%. U and Th concentrations in the rim are also relatively wide and range from 751 to 10184 ppm and 39 to 553 ppm, respectively, which lead to low Th/U ratios (<0.08). Eight analyses yield relatively concentrated $^{206}Pb/^{238}U$ ages ranging from 27.3±0.1 Ma to 28.7±0.9 Ma (Figure 3(e)) and a cluster around 28.2 Ma in a Pb/U concordia diagram, which define a weighted mean age of 28.2±0.5 Ma (MSWD=0.9). Though the rims have low Th/U ratios, well-developed oscillatory overgrowth zoning indicates that they crystallized from granitic melts. Therefore, we interpret this age as the time of crystallization for the Paiku tourmaline leucogranite. Although some ages from the mantle or the rim are similar to data presented as above, they are strongly discordant and plotted to the right of the U/Pb concordia (Figure 3(e)). This suggests that these zircon domains have been influenced by various degrees of Pb loss due to later hydrothermal events.

Sample T0659-B is a representative sample of two-mica granite that consists of quartz, plagioclase, muscovite, biotite, and accessory zircon, apatite, and monazite. Most of zircon grains in this sample are euhedral to subhedral, long prismatic, 100–150 μm long with aspect ratios commonly of 2.0–3.0. Most zircon grains show a similar core-mantle-rim texture in CL and BSE images (Figure 4(a)–(d)). The cores display weak oscillatory zoning (Figure 4(a),(b)) and are surrounded by mantles with typical oscillatory growth zoning, indicative of magmatic origin, and in turn surrounded by sponge-like (Figure 4(b)) or thin grey rims (Figure 4(a),(c),(d)), whereas a few of zircon grains only display core-rim texture (Figure 4(a),(b)).

To constrain the timing of formation of this leucogranites, U/Pb analyses were focused mainly on zircon rims with well-developed oscillatory zoning. Similar to those in sample T0659-A, U and Th concentrations in the cores are highly variable and range from 99 to 1085 ppm and from 3 to 329 ppm, respectively, which results in large variations in Th/U ratios (0.02–0.94). The cores also yield a relatively wide range of $^{206}Pb/^{238}U$ ages from 322.8 to 911.5 Ma (Table 1). Again, they cluster around 481.3 Ma in a Pb/U concordia diagram (Figure 4(e)) and define a weighted mean age of 481.3±4.0 Ma (MSWD=0.1), whereas spots with ages from 322.8 to 414.7 Ma are discordant due to various degrees of Pb loss. The mantles with typical oscillatory growth zoning show similar features in U (110-2991 ppm) and Th (2-439 ppm) concentrations and Th/U ratios (0.01-0.69) to those in the core. Analyses performed on the mantles yield a relatively narrow $^{206}Pb/^{238}U$ age ranging from 19.2±0.3 Ma to 25.6±0.3 Ma (Figure 4(f)), which cluster around 19.8 Ma in a Pb/U concordia diagram and define a weighted mean age of 19.8±0.5 Ma (MSWD=2.3). Due to the well-developed oscillatory overgrowth zoning, we interpret this age as the

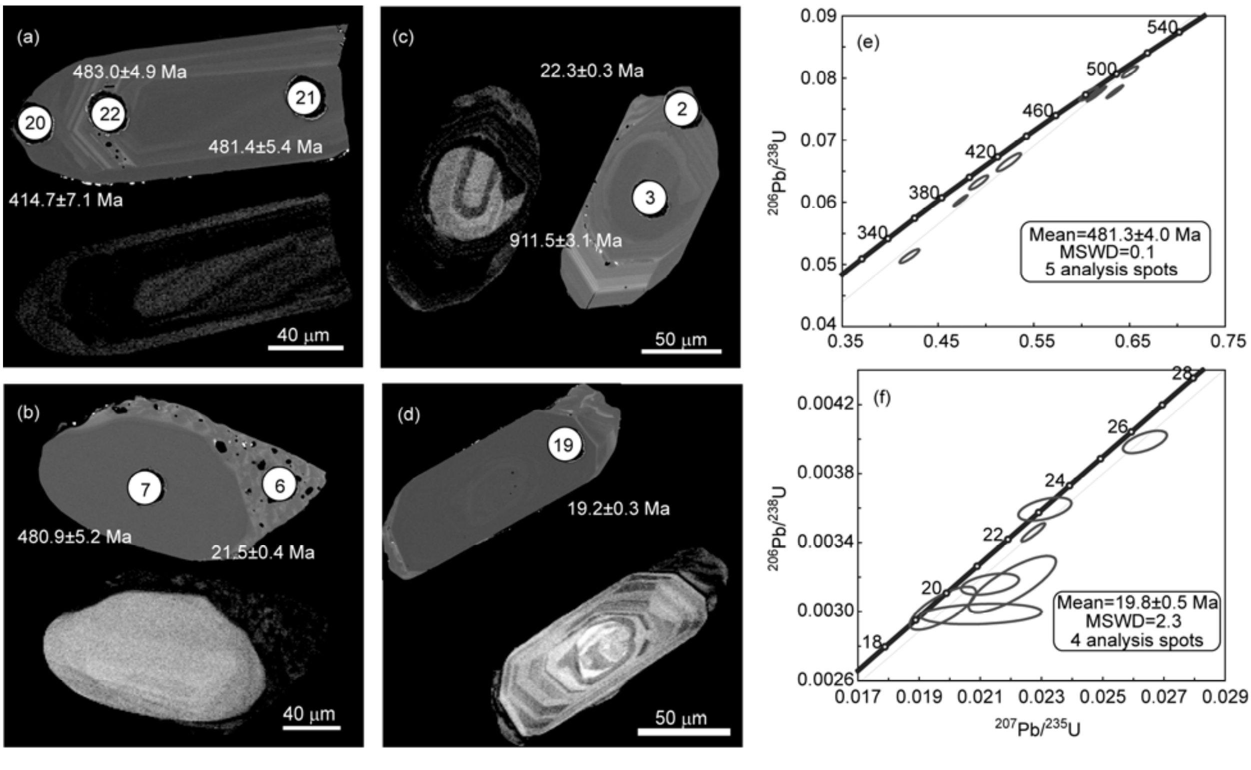

Figure 4 Cathodoluminescence (CL) and Backscatter images (BSE) showing the texture, spot, and respective age of LA-MC-ICP-MS zircon U/Pb dating (a)–(d) and U/Pb concordia diagram (e), (f) for the tourmaline leucogranite T0659-B.

timing of crystallization to form the Paiku two-mica granite. The rims are sponge-like or grey homogenous, indicating that these zircon grains have been affected by later hydrothermal events.

3.2 Zircon Hf isotope geochemistry

We perform in situ zircon Hf isotope analysis on sample T0659-A and T0659-B in order to characterize their Hf isotope compositions of these two types of leucogranite. Some zircon grains with similar textures have no $^{206}Pb/^{238}U$ ages, they are not shown in Figure 5. For our purpose with a focus on the nature of partial melting to produce the Paiku composite leucogranites pluton, we only discriminate analyses on the rim from those either from core or from mantle. Analytical results of zircon grains from the tourmaline leucogranite show that (1) the magmatic rims are characterized by highly heterogenous Hf isotope compositions ($^{176}Hf/^{177}Hf(t)$=0.28237–0.28267, $\varepsilon_{Hf}(t)$=−13.8 to −2.8), and young crustal modal age with T_{DM1}=857−1283 Ma (Figure 5(a), Table 2), and (2) though the core or mantle show similarly wide range in Hf isotope compositions and crustal modal ages, they are substantially more negative ($\varepsilon_{Hf}(t)$=−24.5 to −10.5) and older (T_{DM1}=1169–1662 Ma), respectively (Table 2).

In contrast, Hf analyses on zircon grains from the two-mica granites show different patterns from those in the tourmaline leucogranites. Major differences include (1) relatively smaller variations in the Hf isotope compositions with $^{176}Hf/^{177}Hf(t)$ from 0.28233 to 0.28249 and $\varepsilon_{Hf}(t)$ from −15.0 to −9.3 (Figure 5(b), Table 2) and older crustal modal age T_{DM1} of 1116–1315 Ma from the magmatic rims; (2) much wider range of Hf isotope compositons in cores with $\varepsilon_{Hf}(t)$ from −34.3 to −10.1 and $^{176}Hf/^{177}Hf$ ratio from 0.28179 to 0.28247 (Table 2), and relatively older crustal modal age T_{DM1} of 1120–2041 Ma.

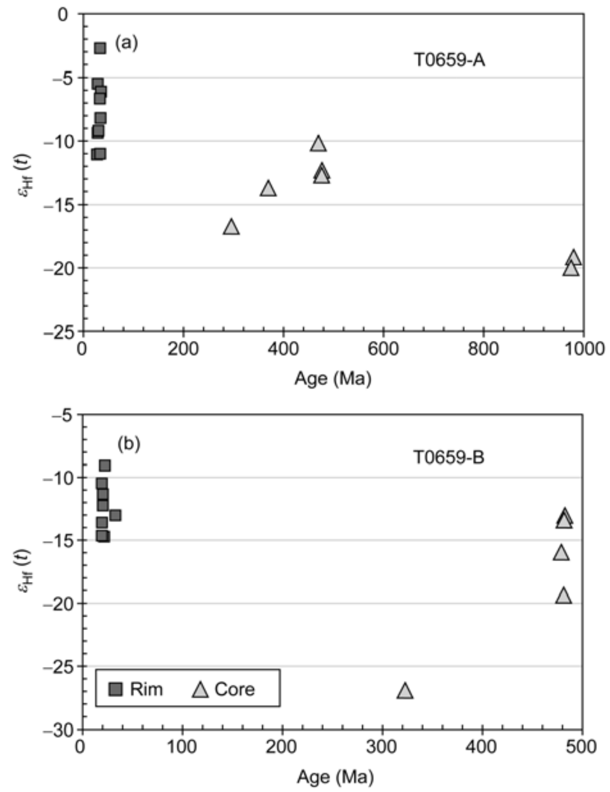

Figure 5 Zircon U/Pb ages and Hf isotope compositions of the tourmaline leucogranite T0659-A (a) and the two-mica granite T0659-B (b) in the Paiku area.

3.3 Buck-rock major and trace element geochemistry

Three types of leucogranite in the Paiku pluton show major differences in major as well as in trace element compositions. Major element abundance is listed in Table 3 and is shown graphically in Figure 6. The tourmaline leucogranites have relatively lower SiO_2 (72.5%–73.2%) than two-mica granites and garnet-bearing leucogranite (73.3%–75.0%), in contrast, the content of Al_2O_3 in the tourmaline leucogranite (>14.8%) is higher than others with Al_2O_3 ranging from 14.3% to 14.8% (Figure 6(a)). As compared to other leucogranites, the tourmaline leucogranite have higher K_2O (>4.9%), lower CaO (<0.7%), and similar contents of Na_2O, FeO, MgO, and MnO (Table 3). Data presented above indicate that all the leucogranites within the Paiku pluton are of K-rich peraluminous granite with A/CNK>1.1 and K_2O> 4.2%.

Similar to major element contents, these leucogranites also show substantial differences in trace element compositions (Figure 7, Table 3). The tourmaline leucogranites contain strikingly highest B (1033–1089 ppm) but lowest Sr concentration (<39 ppm), and the garnet-bearing leucogranite have the lowest Ba concentration among these rocks (Figures 7 and 8(a)). These leucogranites also display similar primitive mantle normalized trace element distribution patterns (Figure 7(a)) characterized by positive anomalies of K and Rb but negative anomalies of Nb, Ti, Sr and Ba. Interestingly, the tourmaline leucogranite show strong positive P anomalies in contrast with negative anomalies in the other types of leucogranite.

All these leucogranites are enriched in light rare earth elements (LREE) and show pronounced negative Eu anomalies except for T0659-12, among which the garnet-bearing ones have the greatest magnitude of negative Eu anomalies. However, heavy rare earth element (HREE) contents in these leucogranites are different. Garnet-bearing leucogranites are weakly enriched in HREE with $(Gd/Yb)_N$=0.6–1.0, whereas the others are weakly depleted in HREE with $(Gd/Yb)_N$=1.5–1.9.

3.4 Sr and Nd isotope geochemistry

In order to characterize the source regimes for these leucogranites within the Paiku pluton, we conduct Sr and Nd isotope analyses on the tourmaline leucogranite and two-

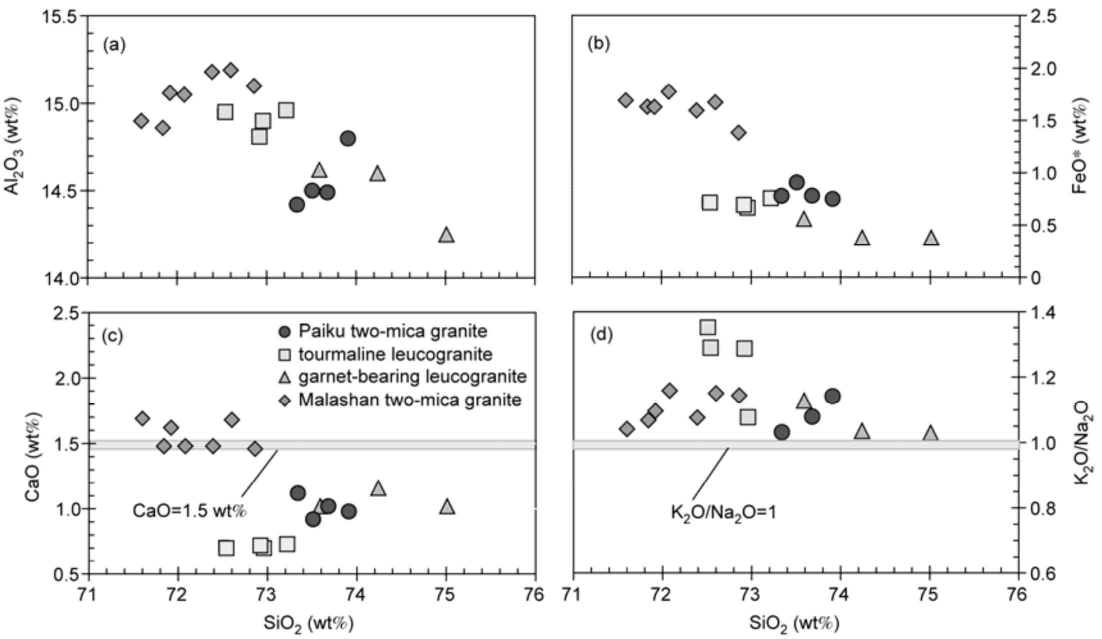

Figure 6 Selected major oxides of (a) Al_2O_3, (b) FeO* and (c) CaO, and (d) K_2O/Na_2O ratio plotted against SiO_2 for the Malashan two-mica granite and the Paiku composite leucogranite.

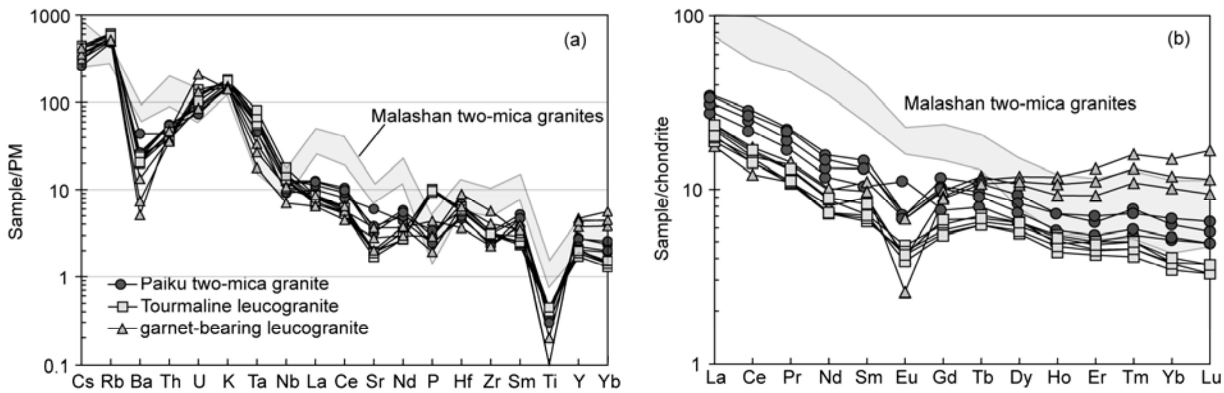

Figure 7 Primitive mantle (PM)-normalized trace element (a) and chondrite-normalized rare earth element (b) distribution patterns for the Malashan two-mica granite and the Paiku composite leucogranite. Primitive mantle and chondrite normalization values are from [43].

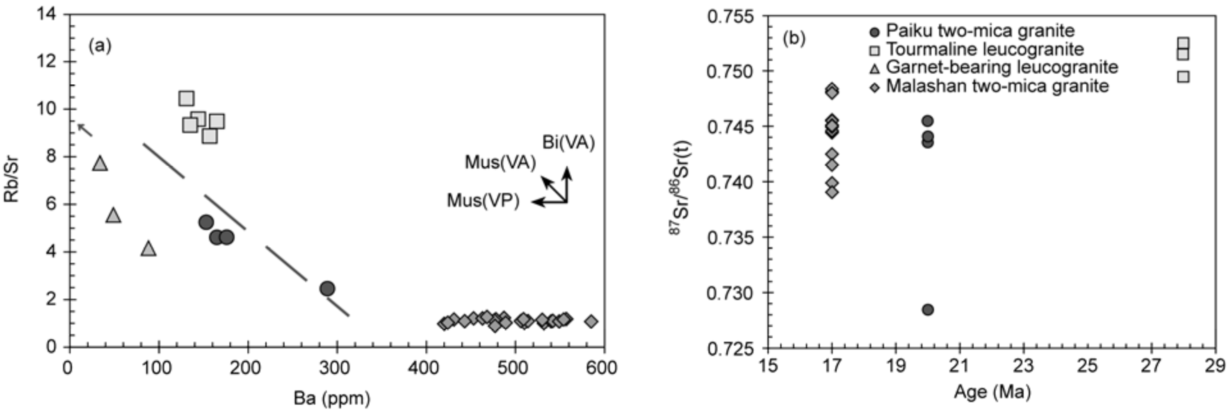

Figure 8 Rb/Sr vs. Ba diagram (a) and $^{87}Sr/^{86}Sr$ vs. age diagram (b) for the Malashan two-mica granite and the Paiku leucogranite.

mica granite. Analytical data are listed in Table 4. Tourmaline leucogranites have relatively higher Rb (>338.0 ppm) and lower Sr (<38.9 ppm), Sm (<4.1 ppm) and Nd (<1.2 ppm) than those in the two-mica granite. The initial Sr isotopic compositions in the tourmaline leucogranites with $^{87}Sr/^{86}Sr(t)$=0.7495–0.7525 are higher than in the two-mica granites with $^{87}Sr/^{86}Sr(t)$=0.7285–0.7454 (Figure 8(b)), whereas both leucogranites are characterized by similarly unradiogenic initial Nd isotopic compositions with $\varepsilon_{Nd}(t)$=−13.0 to −13.3 in the tourmaline leucogranites and $\varepsilon_{Nd}(t)$=−13.4 to −13.9 in the two-mica granites, respectively.

4 Discussions

4.1 Timing of crustal anatexis in the Paiku composite leucogranitic pluton

Previous studies considered the Paiku leucogranitic pluton as a single pluton [24–26], and reported its crystalline ages of 22.2–16.2 Ma [25]. Such a wide age span could be due to analysis on zircon domains straddling cross different overgrowth zoning. Field investigations, petrographic examinations (Figure 2), geochemical analyses (Figures 6–8) and updated zircon U/Pb dating (Figures 3–5) all demonstrate that the Paiku pluton is a composite pluton consisting of tourmaline leucogranite, two-mica granite, and garnet-bearing leucogranite.

Zircon grains in the tourmaline leucogranite show a well-preserved core-mantle-rim texture. Inherited cores show two dominant age groups at ~483.3 and ~851.0 Ma. Mantles with $^{206}Pb/^{238}U$ age of 33.6±0.6 Ma are characterized by either weak oscillatory overgrowth zoning indicative of zircon growth from granitic melts or by grey homogenous texture from metamorphic recrystallization (Figure 3(a)–(d)) and low Th/U ratios (<0.11). The co-existence of these zircon overgrowth textures in the mantle domains at 33.6±0.6 Ma indicates that the source regime for the tourmaline leucogranite had experienced metamorphism under P-T conditions higher enough to induce partial melting at the same time. This event could correspond to crustal anatexis at ~35.3 Ma during the tectonic transition from compressive shortening to extension in the Yardoi dome at the eastmost of NHGD [12], migmatization at 35.0±0.8 Ma in the Mabja Dome [19], and the earliest phase of partial melting at 36.5±2.2 Ma recorded in the deformed granites within the STDS in the Gyirong areas [20]. Similar to zircon grains from leucogranites along the Himalayan belt, zircons from sample T0659-A also contain up to 2000 ppm U. Due to radioactive decay of U, such zircons experienced extensive destruction and recrystallization and develop sponge-like textures. However, the well-developed typical oscillatory overgrowth zoning in most rims indicates that they crystallized from granitic melts. These domains yield relatively low Th/U ratios from 0.02 to 0.08, characteristics of anatectic zircons. Therefore, The $^{206}Pb/^{238}U$ age of 28.2±0.5 Ma represents the timing of crystallization to form the tourmaline leucogranite, similar to that of Kuday granites at 27.5±0.5 Ma in the central NHGD [44].

Zircons in the two-mica granites also show a core-mantle-rim texture. The inherited zircon cores show weak oscillatory zoning (Figure 4(a), (b)) and yield dominant $^{206}Pb/^{238}U$ age group at 481.3±4.0 Ma. This indicates that the source regime consists of major components that contributed from ~481 Ma magmatic events. The mantle domains are of typical oscillatory overgrowth zoning (Figure 4(c), (d)), characteristics of magmatic origin, and yield $^{206}Pb/^{238}U$ ages clustered at 19.8±0.5 Ma. This age represents the time to crystallize the two-mica granite. However, sponge-like textures and thin grey homogenous rims suggest that these rocks have been affected by later hydrothermal activities.

In summary, data presented above indicate that the tourmaline leucogranite formed at 28.2±0.5 Ma and its source regime experienced high metamorphism and simultaneous partial melting at 33.6±0.6 Ma, whereas the two-mica granite formed at 19.8±0.5 Ma. Therefore, the Paiku leucogranitic pluton is a composite pluton built by episodic intrusions over a time span of ~8 myr.

4.2 Source rock of the Paiku composite leucogranite

Date presented above indicate that: (1) the Paiku leucogranite is a composite pluton and consists of tourmaline leucogranite, two-mica granite and garnet-bearing leucogranite; (2) the tourmaline leucogranite formed earlier at ~28.2 Ma and its source rock experienced high metamorphism and simultaneous anatexis at ~33.6 Ma, in contrast to much later for the two-mica granite at ~19.8 Ma; (3) though the amount of analyses on the zircon cores are too limited to fully cover the age spectrum of inherited zircon, two types of leucogranite both contain a large number of ~480 Ma inherited zircons. This implies that their source rocks might have major contributions from the Ordovician magmatic event, possibly in a continental arc environment [45]; (4) the bulk-rock initial Sr isotope compositions and zircon Hf isotope compositions in the tourmaline leucogranites are higher than those in the two-mica granites; (5) all three types of leucogranite are of K-rich peraluminous with A/CNK>1.1 and show slight differences in major element compositions (e.g. SiO_2, Al_2O_3, and CaO); (6) the tourmaline leucogranites have extraordinary high B concentrations and positive P anomalies; and (7) both the tourmaline leucogranites and the two-mica granites are enriched in LREE, but depleted in HREE and show negative Eu anomalies, in contrast, garnet-bearing leucogranites are not only enriched in LREE but also slightly enriched in HREE and show strongest negative Eu anomalies among all these rocks.

Previous studies on the timing of crustal anatexis in the Himalayan orogenic belt indicated that leucogranites formed at 27–10 Ma in the NHGD and the HHCS are typical S-type granites, derived from muscovite dehydration melting of metapelites and characterized by high initial $^{87}Sr/^{86}Sr$ ratios of 0.7300–0.7800 and low ε_{Nd} from −10 to −15 [1–7,16,46,47]. Experimental results [6,7], theoretic calculations [22,23] and field investigations [4,16,18] all suggest that fertile metapelites could undergo progressive partial melting with variations in temperature, pressure, and water content, which leads to the formation of granites with different geochemical characteristics in major and trace element as well as in isotope (e.g. Sr, Nd) geochemistry. Metapelites rich in mica, plagioclase, and quartz are fertile crustal material and could produce granitic melts through muscovite- or biotite-melting reactions at fluid-present as well as fluid-absent conditions. The degree of melting at optimum P-T-X conditions can amount to 40 %, but it decreases significantly at low temperature of ~700°C. Through continuous or discontinuous melting reactions, melts from the same metapelite could potentially show complex Rb-Sr system relationship [22,48]. Recent petrologic and geochemical studies on the mid-Miocene Malashan TMG demonstrate that they were derived from fluxed melting of muscovite [17]. These granites are characterized by higher contents of CaO (>1.5%, Figure 6) and Ba (Figure 7), but lower and nearly constant Rb/Sr ratios (<1.4) relative to large variations in Ba concentrations (Figure 8(a)). Leucogranites in the Paiku composite pluton show different geochemical nature from those in the Malashan TMG, but similar to typical Himalayan Cenozoic leucogranites (Figures 6 and 7). Negative correlationship between Rb/Sr and Ba (Figure 8(a)) in the Paiku leucogranites suggests that they were derived from muscovite dehydration melting of metapelites. The initial Sr and Nd isotope compositions in these Paiku leucogranites are different. Sr isotope compositions in the tourmaline leucogranites are slightly higher than those in the two-mica granites, but they both have similarly low ε_{Nd} values. Factors that could contribute to the observed geochemical and isotopic features in the Paiku leucogranites include: (1) distinct source rocks, (2) difference in proportion of muscovite involved in the partial melting reactions, or (3) both effects.

Experimental results and theoretic calculations demonstrate that as compared with muscovite dehydration melting, proportion of muscovite involved in the fluxed melting of muscovite reactions decrease substantially accompanied by increase in feldspar components, which results in melts with enhanced contents of Sr, but lower Rb, Rb/Sr ratios and Sr isotope compositions [7,22,44]. As compared with the Paiku two-mica granites, the tourmaline leucogranites have higher Rb/Sr ratios and Sr isotope compositions, implying that much more muscovite involved in the dehydration melting of metapelites to generate the tourmaline leucogranites. However, only differences in partial melting reactions can not explain the large variations in Sr isotope compositions of the two-mica granites ranging from 0.728477 to 0.745432 and relatively lower Hf isotope compositions. Therefore, except for distinct crystallization ages of the two types of leucogranites, their source rocks maybe different.

If the tourmaline leucogranites and the two-mica granites have same source rock, they should have show the following features including (1) similar age spectrum in inherited zircon cores; (2) higher initial Sr but lower initial Nd isotope compositions in the two-mica granites than those in the tourmaline leucogranite; and (3) Hf isotope compositions in magmatic zircon rims should increase with the decrease of crystallization ages. The zircon textures (Figures 3 and 4) and U/Pb ages (Figure 9, Table 1) indicate that both leucogranites contain ~480 Ma inherited zircons, but the tourmaline leucogranites contain much older (up to 1922.4 Ma) inherited zircon grains than the two-mica granites. In addition, Hf isotope compositions in inherited zircons from both leucogranites are substantially different (Figure 5). Inherited zircons from the tourmaline leucogranites have higher $\varepsilon_{Hf}(t)$ ranging from −24.5 to −10.5 and younger crustal modal ages of 1169–1662 Ma in contrast with much lower $\varepsilon_{Hf}(t)$ and older crustal modal age of inherited zircons in the two-mica granite. Differences in Sr and Hf isotope compositions between the tourmaline leucogranites and the two-mica granites (Figures 5 and 8) indicate that they could not share the same source rocks, consistent with inference drawn from Rb/Sr-Ba systematics. However, similar Nd isotope compositions in both leucogranites imply that Sm-Nd isotope system is more robust than Rb-Sr system which is more susceptible to be perturbed by metamorphism or hydrothermal reactions. Within the Himalayan orogenic belt, data from literature [13] and to be published of metamorphic rocks demonstrate that the mineral assemble and bulk-rock major and trace element compositions of metapelites

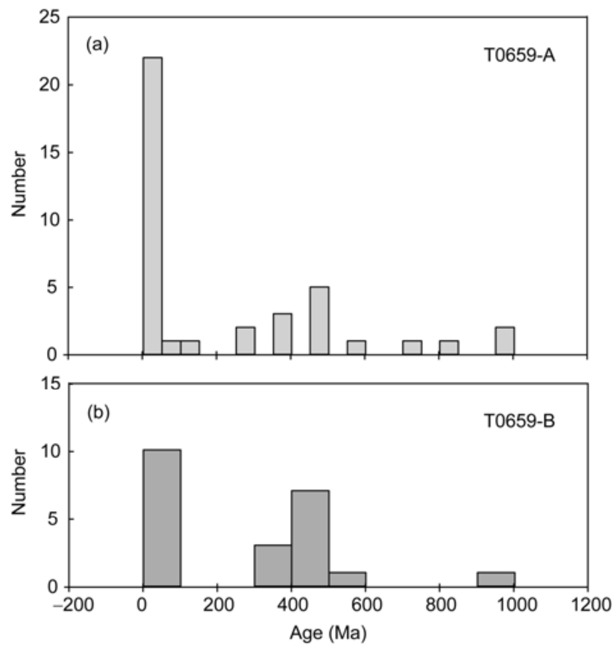

Figure 9 Age comparison between tourmaline leucogranite T0659-A (a) and two-mica granite T0659-B (b) in the Paiku area.

are highly heterogeneous. Such metapelites could potentially undergo partial melting at various temperature and pressure conditions during the tectonic evolution of the Himalayan orogen and produced distinct leucogranitic melts. Data presented above demonstrate that metasedimentary rocks, presumably at the middle to lower crustal levels, had experienced episodic melting at ~33.6, ~28.2, and ~19.8 Ma, respectively, among which the later two correspondently produced the tourmaline leucogranite and two-mica granite in the Paiku pluton. Despite difference in the formation ages, different source regimes and different partial melting reactions together lead to the pronounced geochemical heterogeneity in these leucogranites.

4.3 The implication of melting in Paiku composition leucogranite

Both detailed structural investigations and geochronologic studies indicate that the Malashan, Kangmar, and Mabja gneiss domes had experienced similar types of metamorphism and deformation [19,24–26,32,49,50], which strongly suggest that they were formed in the same tectonic setting [21]. Lee et al. [19] documented that the migmatites in the Mabja gneiss dome had experienced partial melting at 35.0±0.8 Ma. Within the Yardoi gneiss dome, recent studies found a suite of ~43 Ma high Sr/Y two-mica granites and ~35 Ma high Na/K leucogranites [12,13]. These granites represent the melting products from amphibolite at thickened crustal conditions and during the tectonic transition from compressive shorting to extension in the Himalayan orogen, respectively. In addition, syn-collision leucogranites within the STDS in the Gyirong area also record partial melting at ~36 Ma [20]. These studies suggest that there is strong genetic relationship between middle to lower crustal anatexis represented by formation of granites and large scale of extensional deformation. Initiation of the STDS could be triggered by these ~35 Ma melting processes and traced back to ~35 Ma [12,19–21]. In this contribution, geochronological and geochemical characteristics of the Paiku leucogranites in the Malashan area indicate that crustal anatexis in the western NHGD could be as early as 33.6±0.6 Ma or older, similar to the central and eastern NHGD. Partial melting of distinct metapelites in response to the evolving P-T-X conditions during the tectonic evolution of large collisional orogenic belts indeed could generate a spectrum of granitic melts with distinct geochemical as well as isotopic characteristics. The earliest anatexis both at the hanging wall and footwall of the STDS in the Himalaya collisional belt occurred at 35 Ma, indicating that ~35 Ma partial melting may be the major factor to initiate the STDS and in turn leads to tectonic transition from compressive shortening to extension. Within the Tibetan plateau and adjacent areas, initial movement of the Karakorum Fault [51], large displacement along the Altyn Tagh fault [52,53], strike-slip movements in the Red River belt [54], and aridification of the Tibetan plateau linked to global cooling [55] all occurred at ~35 Ma. All these studies indicate that ~35 Ma tectonic events in the Tibetan plateau are widespread. Under intensive compression, the southern Tibet experienced tectonic transition at ~ 35 Ma from compressive shortening to extension. In the Malashan area, the tourmaline leucogranite and two-mica granite formed at ~28.2 and ~19.8 Ma, respectively, corresponding to two main phases of partial melting at 26 Ma and at 21–20 Ma recorded in the syn-collision granites within the STDS [20] and coinciding with the active time of STDS from 25 to 12 Ma [56–60]. Therefore, formation of the Oligocene and mid-Miocene leucogranites in the Paiku area suggests that movement along the STDS not only triggered rapid exhumation of high grade metamorphic rocks but also induced large-scale crustal anatexis.

Combined with literature data, we suggest that prior to 35 Ma, the Himalayan orogenic belt underwent intensive shortening accompanied by partial melting of middle-lower crustal material. These melting processes effectively changed physical properties of deep crustal rocks and triggered the tectonic transition of the Himalayan orogen from compression to extension and initiated the movement of the STDS. With further extension along the STDS, rapid exhumation of deep crustal materials resulted in the large-scale decompression melting of metapelites and the formation of typical Himalayan S-type granites with ages <30 Ma [13,19–21]. The Oligocene (~28 Ma) and mid-Miocene (~20 Ma) leucogranites in the Paiku area represent the melting products from metapelites associated with the active movement along the STDS.

We thank the editors for handling this manuscript carefully and two anonymous reviews for their constructive comments which greatly improved the manuscript. This work was supported by the National Basic Research Program of China (*2011CB403102*) *and the National Natural Science Foundation of China* (*41073024 and 41273034*).

1 Harris N, Massey J. Decompression and anatexis of Himalayan metapelites. Tectonics, 1994, 13: 1537–1546
2 Harris N, Ayres M, Massey J. Geochemistry of granitic melts produced during the incongruent melting of muscovite-implications for the extraction of Himalayan leucogranite magmas. J Geophys Res, 1995, 100: 15767–15777
3 Harrison T M, Oscar M L, Marty G, et al. New insight into the origin of two contrasting Himalayan granite belts. Geology, 1997, 25: 899–902
4 Zhang H F, Harris N, Parrish R, et al. Causes and consequences of protracted melting of the mid-crust exposed in the North Himalayan antiform. Earth Planet Sci Lett, 2004, 228: 195–212
5 Le Fort P. Manaslu leucogranite: A collision signature of the Himalaya a model for its genesis and emplacement. J Geophys Res, 1981, 86: 10545–10568
6 Patiño Douce A E, Harris N. Experimental constraints on Himalayan Anatexis. J Petrol, 1998, 39: 689–710
7 Knesel K M, Davidson J P. Insight into collisional magmatism from isotopic fingerprints of melting reactions. Science, 2002, 296: 2206–2208
8 Aikman A B, Harrison T M, Ding L. Evidence for Early (>44 Ma) Himalayan Crustal Thickening, Tethyan Himalaya, southeastern Tibet.

Earth Planet Sci Lett, 2008, 274: 14–23
9 Gao L E, Zeng L S, Liu J, et al. Early Oligocene Na-rich peraluminous leucogranites in the Yardoi gneiss dome, southern Tibet: Formation mechanism and tectonic implications (in Chinese). Acta Petrol Sin, 2009, 25: 2289–2302
10 Gao L E, Zeng L S, Hu G Y. High Sr/Y two-mica granite from Quedang, southern Tibet, China: Formation mechanism and tectonic implications (in Chinese). Geol Bull Chin, 2010, 29: 214–226
11 Xie K J, Zeng L S, Liu J. et al. Late-Eocene Dala adalitic granite, southern Tibet and geological implication (in Chinese). Acta Petrol Sin, 2010, 26: 1016–1026
12 Zeng L S, Liu J, Gao L E, et al. Early Oligocene crustal anatexis in the Yardoi gneiss dome, southern Tibet and geological implications. Chin Sci Bull, 2009, 54: 104–112
13 Zeng L S, Gao L E, Xie K J, et al. Mid-Eocene high Sr/Y granites in the Northern Himalayan Gneiss Domes: Melting thickened lower continental crust. Earth Planet Sci Lett, 2011, 303: 251–266
14 Hou Z Q, Zheng Y C, Zeng L S, et al. Eocene-Oligocene granitoids in southern Tibet: Constraints on crustal anatexis and tectonic evolution of the Himalayan orogen. Earth Planet Sci Lett, 2012, 349–350: 38–52
15 Prince C, Harris N, Vance D. Fluid-enhanced melting during prograde metamorphism. J Geol Soc Lon, 2001, 158: 233–241
16 King J, Harris N, Argles T, et al. The contribution of crustal anatexis to the tectonic evolution of Indian crust beneath southern Tibet. Geol Soc Amer Bull, 2011, 123: 218–239
17 Gao L E, Zeng L S. Mid-Miocene two-mica granites in the Malashan gneiss dome, south Tibet: Geochemical characteristics and formation mechanism. Abstract presented at 2011 AGU Fall Meeting, 2011, Dec 5–9, San Francisco
18 Zeng L S, Gao L E, Dong C Y, et al. High-pressure melting of metapelite and the formation of Ca-rich granitic melts in the Namche Barwa Massif, southern Tibet. Gondwana Res, 2012, 21: 138–151
19 Lee J, Whitehouse M J. Onset of mid-crustal extensional flow in southern Tibet: Evidence from U/Pb zircon ages. Geology, 2007, 35: 45–48
20 Yang X Y, Zhang J J, Qi G W. Structure and deformation around the Gyirong basin, northern Himalaya, and onset of the south Tibetan detachment system. Sci China Ser D-Earth Sci, 2009, 52: 1046–1058
21 Zhang J J, Yang X Y, Qi G W, et al. Geochronology of the Malashan dome and its application in formation of the Southern Tibet detachment system (STDS) and Northern Himalayan gneiss domes (NHGD) (in Chinese). Acta Petrol Sin, 2011, 27: 3535–3544
22 Zeng L S, Asimow P, Saleeby J B. Coupling of anatectic reactions and dissolution of accessory phases and the Sr and Nd Isotope systematics of anatectic melts from a metasedimentary source. Geochim Cosmochim Acta, 2005, 69: 3671–3682
23 Zeng L S, Saleeby J B, Asimow P. Nd isotope disequilibrium during crustal anatexis: A record from the Goat Ranch migmatite complex, southern Sierra Nevada batholith, California. Geology, 2005, 33: 53–56
24 Aoya M, Wallis S R, Kawakami T, et al. The Malashan metamorphic complex in southern Tibet: Dominantly top-to the-north deformation and intrusive origin of its associated granites. Himalayan Journal of Science, 2004, 2: 92
25 Kawakami T, Aoya M, Wallis S R, et al. Contact metamorphism in the Malashan Dome, North Himalayan gneiss domes, southern Tibet: an example of shallow extensional tectonics in the Tethys Himalaya. J Metamorphic Geol, 2007, 25: 831–853
26 Aoya M, Wallis S R, Terada K, et al. North-south extension in the Tibetan crust triggered by granite emplacement. Geology, 2005, 33: 853–856
27 Debon F, Le Fort P, Sheppard S, et al. The four plutonic belts of the Transhimalaya-Himalaya: A chemical, mineralogical, isotopic, and chronological synthesis along a Tibet-Nepal Section. J Petrol, 1986, 27: 219–250
28 Harrison T M, Grove M, Lovera O M, et al. The origin of Himalayan anatexis and inverted metamorphism: Models and constraints. J Asian Earth Sci, 1999, 17: 755–772
29 Gao L E, Zeng L S, Xie K J. Eocene high grade metamorphism and crustal anatexis in the North Himalaya Gneiss Domes, Southern Tibet. Chin Sci Bull, 2012, 57: 639–650
30 Schärer U, Xu R, Allegre C. U-(Th)-Pb systematics and ages of Himalayan leucogranites, south Tibet. Earth Planet Sci Lett, 1986, 77: 35–48
31 Pan G T, Ding J. 1∶1500000 Geologic map of the Tibetan Plateau and adjacent areas. 2004
32 Lee J, Hacker B R, Dinklage W S, et al. Evolution of the Kangmar dome, southern Tibet: Structural, petrologic and thermochronologic constraints. Tectonics, 2000, 19: 872–895
33 Hou K J, Li Y H, Tian Y Y. *In situ* U-Pb zircon dating using laser ablation-multi ion couting-ICP-MS. Mineral Deposits, 2009, 28: 481–492
34 Nasdala L, Hofmeister W, Norberg N, et al. Zircon M257−a homogeneous natural reference material for the ion microprobe U-Pb analysis of zircon. Geostand Geoanal Res, 2008, 32: 247–265
35 Jackson S E, Pearson N J, Griffin W L, et al. The application of laser ablation-inductively coupled plasma-mass spectrometry to *in situ* U-Pb zircon geochronology. Chem Geol, 2004, 211: 47–69
36 Liu Y S, Gao S, Hu Z C, et al. Continental and oceanic crust recycling-induced melt-peridotite interactions in the Trans-North China Orogen: U-Pb dating, Hf isotopes and trace elements in zircons from mantle xenoliths. J Petrol, 2010, 51: 537–571
37 Ludwig K R. ISOPLOT: A geochronological toolkit for Microsoft Excel. Berkeley Geochronol Center Spec Publ, 2003, 4: 71
38 Hou K J, Li Y H, Zou T R, et al. Laser ablation-MC-ICP-MS technique for Hf isotope microanalysis of zircon and its geological applications (in Chinese). Acta Petrol Sin, 2007, 23: 2595–2604
39 Chu N C, Taylor R N, Chavagnac V, et al. Hf isotope ratio analysis using multi-collector inductively coupled plasma mass spectrometry: An evaluation of isobaric interference corrections. J Anal At Spectrom, 2002, 17: 1567–1574
40 Wu F Y, Yang Y H, Xie L W, et al. Hf isotopic compositions of the standard zircons and baddeleyites used in U–Pb geochronology. Chem Geol, 2006, 234: 105–126
41 Morel M L A, Nebel O, Nebel-Jacobsen Y J, et al. Hafnium isotope characterization of the GJ-1 zircon reference material by solution and laser-ablation MC-ICPMS. Chem Geol, 2008, 255: 231–235
42 Sláma J, Kosler J, Condon D J, et al. Plesovice zircon: A new nature reference material for U-Pb and Hf isotopic microanalysis. Chem Geol, 2008, 249: 1–35
43 Sun S S, McDonough W F. Chemical and isotopic systematics of oceanic basalts: Implications for mantle composition and processes. Geol Soc Spec Publ, 1989, 42: 313–345
44 Zhang H F, Harris N, Parrish R, et al. U-Pb ages of Kude and Sajia leucogranites in Sajia dome from North Himalaya and their geological implications. Chin Sci Bull, 2004, 49: 2087–2092
45 Cawood P A, Buchan C. Linking accretionary orogenesis with supercontinent assembly. Earth-Sci Rev, 2007, 82: 217–256
46 Daniel C, Vidal P, Fernandez A, et al. Isotopic study of the Manaslu granite (Himalaya, Nepal): Inferences of the age and source of Himalayan leucogranites. Contrib Mineral Petrol, 1987, 96: 78–92
47 Inger S, Harris N. Geochemical Constraints on Leucogranite Magmatism in the Langtang Valley, Nepal Himalaya. J Petrol, 1993, 34: 345–368
48 Harris N B W, Inger S. Trace element modeling of pelite-derived granites. Contrib Mineral Petrol, 1992, 110: 46–56
49 Lee J, Hacker B, Wang Y. Evolution of North Himalayan Gneiss Domes: Structural and metamorphic studies in Mabja Dome, southern Tibet. J Struct Geol, 2004, 26: 2297–2316
50 Lee J, McClelland W, Wang Y, et al, Oligocene-Miocene middle crustal flow in southern Tibet: Geochronologic studies in Mabja Dome. Geol Soc Spec Publ, 2006, 268: 445–470
51 Li H B, Valli F, Liu D Y, et al. Initial movement of the Karakorum Fault in western Tibet: Constraints from SHRIMP U-Pb dating of zircon. Chin Sci Bull, 2008, 52: 1089–1100
52 Meng Q R, Hu J M, Yang F Z. Timing and magnitude of displacement on the Altyn Tagh fault: Constraints from stratigraphic correla-

tion of adjoining Tarim and Qaidam basins, NW China. Terra Nova, 2003, 13: 86–91
53 Guo Z J, Lu J M, Zhang Z C. Cenozoic exhumation and thrusting in the northern Qilian Shan, northeastern margin of the Tibetan Plateau: Constraints from sedimentological and apatite fission-track Data. Acta Geol Sin, 2009, 83: 801–840
54 Schärer U, Zhang L S, Tapponnier P. Duration of strike-slip movements in large shear zones: The Red River belt, China. Earth Planet Sci Lett, 1994, 126: 379–397
55 Dupont-Nivet G, Krijgsman W, Langereis C G, et al. Tibetan plateau aridification linked to global cooling at the Eocene-Oligocene transition. Nature, 2007, 445: 635–638
56 Hodges K V. Tectonics of the Himalaya and southern Tibet from two perspectives. Geol Soc Am Bull, 2000, 112: 324–350
57 Yin A, Harrison T M. Geologic evolution of the Himalayan-Tibetan orogen. Annu Rev Earth Planet Sci, 2000, 28: 211–280
58 Hurtado J M, Hodges K V, Whipple K X. Neotectonics of the Takkhola Graben and implications for recent activity on the South Tibetan Fault System in the central Nepalese Himalaya. Geol Soc Am Bull, 2001, 113: 222–240
59 Searle M P, Godin L. The south Tibetan detachment and the Manaslu leucogranite: A structural reinterpretation and restoration of the Annapurna-Manaslu Himalaya, Nepal. J Geol, 2003, 111: 505–523
60 Yin A. Cenozoic tectonic evolution of the Himalayan orogen as constrained by along-strike variation of structural geometry, exhumation history, and foreland sedimentation. Earth Sci Rev, 2006, 76: 1–131